

ARTICLE

Received 28 Jul 2015 | Accepted 11 Mar 2016 | Published 13 Apr 2016

DOI: 10.1038/ncomms11329

OPEN

Magnetic hyperbolic optical metamaterials

Sergey S. Kruk¹, Zi Jing Wong², Ekaterina Pshenay-Severin^{1,3}, Kevin O'Brien², Dragomir N. Neshev¹, Yuri S. Kivshar¹ & Xiang Zhang^{2,4,5}

Strongly anisotropic media where the principal components of electric permittivity or magnetic permeability tensors have opposite signs are termed as hyperbolic media. Such media support propagating electromagnetic waves with extremely large wave vectors exhibiting unique optical properties. However, in all artificial and natural optical materials studied to date, the hyperbolic dispersion originates solely from the electric response. This restricts material functionality to one polarization of light and inhibits free-space impedance matching. Such restrictions can be overcome in media having components of opposite signs for both electric and magnetic tensors. Here we present the experimental demonstration of the magnetic hyperbolic dispersion in three-dimensional metamaterials. We measure metamaterial isofrequency contours and reveal the topological phase transition between the elliptic and hyperbolic dispersion. In the hyperbolic regime, we demonstrate the strong enhancement of thermal emission, which becomes directional, coherent and polarized. Our findings show the possibilities for realizing efficient impedance-matched hyperbolic media for unpolarized light.

¹Nonlinear Physics Center and Center for Ultrahigh Bandwidth Devices for Optical Systems (CUDOS), Research School of Physics and Engineering, The Australian National University, Canberra, Australian Capital Territory 2601, Australia. ²NSF Nanoscale Science and Engineering Center, University of California, Berkeley, California 94720, USA. ³Institute of Applied Physics, Abbe Center of Photonics, Friedrich-Schiller-Universität Jena, 07743 Jena, Germany. ⁴Materials Sciences Division, Lawrence Berkeley National Laboratory, Berkeley, California 94720, USA. ⁵Department of Physics, King Abdulaziz University, Jeddah 21589, Saudi Arabia. Correspondence and requests for materials should be addressed to S.S.K. (email: Sergey.Kruk@anu.edu.au).

The study of hyperbolic media and hyperbolic metamaterials have attracted significant attention in recent years due to their relatively simple geometry and many interesting properties, such as high density of states, all-angle negative refraction and hyperlens imaging beyond the diffraction limit^{1–3}. Usually, both artificial^{4–9} and natural^{10,11} media with hyperbolic dispersion are uniaxial materials whose axial and tangential dielectric permittivities have opposite signs. In general, however, the propagation of electromagnetic waves inside a material is defined by both the dielectric permittivity and magnetic permeability tensors. Specifically, the electric response defines the dispersion for the transverse magnetic (TM) linearly polarized light, and the magnetic response defines the dispersion for transverse electric (TE) polarization (see details in Supplementary Note 1). Therefore, the ability to control both the electric permittivity and magnetic permeability gives a full flexibility for the dispersion engineering for any arbitrary polarization and nonpolarized light. This is of a major importance for the efficient interaction with randomly positioned emitters or thermal radiation. Moreover, a control over both electric and magnetic responses allows one to engineer the material dispersion and impedance independently, and, in particular, to achieve impedance matching between a hyperbolic material and the free space. Impedance matching prevents any light reflections at the interfaces and allows for efficient light coupling and extraction from the hyperbolic materials. Therefore, the development of magnetic hyperbolic materials with a simultaneous control over both dielectric permittivity and magnetic permeability tensors remains an important milestone. In particular, it is of a special interest to realize experimentally a magnetic hyperbolic material with the effective magnetic permeability tensor having principal components of the opposite signs^{1,12}. Such a development would open new opportunities for super-resolution imaging, nanoscale optical cavities or control over the density of photon states and, in particular, the magnetic density of states for enhancing brightness of magnetic emitters^{13,14}.

In recent years, we have seen the development of numerous structures with artificial magnetism. However, these structures are largely limited to planar metasurfaces of deeply subwavelength thickness. Importantly, many properties and functionalities of hyperbolic media rely on wave propagation inside them and therefore require essentially a three-dimensional design. For example, hyperlens super-resolution imaging relies on conversion of evanescent waves propagating in a bulk of hyperbolic media^{15,16}. Nowadays, the realization of three-dimensional metamaterial structures¹⁷ is at the edge of technological possibilities associated with extreme fabrication difficulties and material constraints. To date, no photonic

structures with hyperbolic dispersion in the magnetic response have been demonstrated, and such types of structures are only known for microwave systems^{18,19}.

Here we demonstrate experimentally optical magnetic hyperbolic metamaterial with principal components of the magnetic permeability tensor having the opposite signs. We directly observe a topological transition between the elliptic and hyperbolic dispersions in metamaterials. In the hyperbolic regime, the length of wave vectors inside the metamaterial is diverging towards infinity. We reveal the effect of the hyperbolic dispersion on thermal emission, where the magnetic hyperbolic metamaterial demonstrates enhanced, directional, coherent and polarized thermal emission. Our experimental observations are supported by analytical calculations as well as full-wave numerical simulations.

Results

Sample fabrication. To realize a magnetic hyperbolic medium in optics, we employ multilayer fishnet metamaterials, known as the bulk-type metamaterials with negative refractive index at optical frequencies²⁰. Multilayer fishnets were predicted theoretically to possess a magnetic hyperbolic dispersion²¹, but direct measurements of their dispersion remained out of reach. To test this, we fabricate a fishnet metamaterial by using focused ion beam milling through a stack of 20 alternating films of gold and magnesium fluoride (see details in Methods). The sample is fabricated on a 50-nm-thin silicon nitride membrane. A sketch and scanning electron microscopy image of the fabricated structure are shown in Fig. 1. The fishnets feature high optical transmission in the near-infrared spectral region, exhibiting a transmission maximum of 42% at $\sim 1,320$ nm wavelength, as shown in Fig. 1b. We also measure the fishnet refractive index at normal incidence using spectrally and spatially resolved interferometry²². The fishnet's refractive index shown in Fig. 1c is constantly decreasing with an increase of the wavelength exhibiting negative values at wavelengths above 1,410 nm.

Angular dispersion measurements. To reconstruct the dispersion isofrequency contours experimentally, we determine the length of the k -vectors of light inside the materials for a range of different directions. For this, we measure both amplitude and phase of the transmitted and reflected light, and find the k -vectors via the reverted Fresnel equations (see details in Supplementary Note 2).

For the phase measurements, we employ interferometry techniques. Specifically, for measuring a phase in transmission,

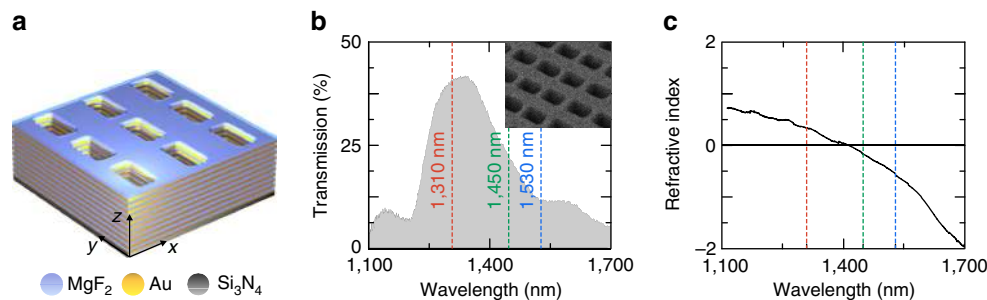


Figure 1 | Multilayer fishnet metamaterial. (a) Sketch of the structure. Thicknesses of MgF₂ and Au layers are 45 and 30 nm, respectively. Thickness of Si₃N₄ membrane is 50 nm. Lattice period is 750 × 750 nm. Size of holes is 260 × 530 nm. (b) Experimentally measured transmission spectrum of the fishnet metamaterial. Inset shows a scanning electron microscopy image of the fabricated structure. (c) Effective refractive index of the fishnet metamaterial extracted for the normal incidence. The marked lines in **b** and **c** represent the wavelengths in the regions of elliptic dispersion (red), crossover optical topological transition (green) and hyperbolic dispersion (blue).

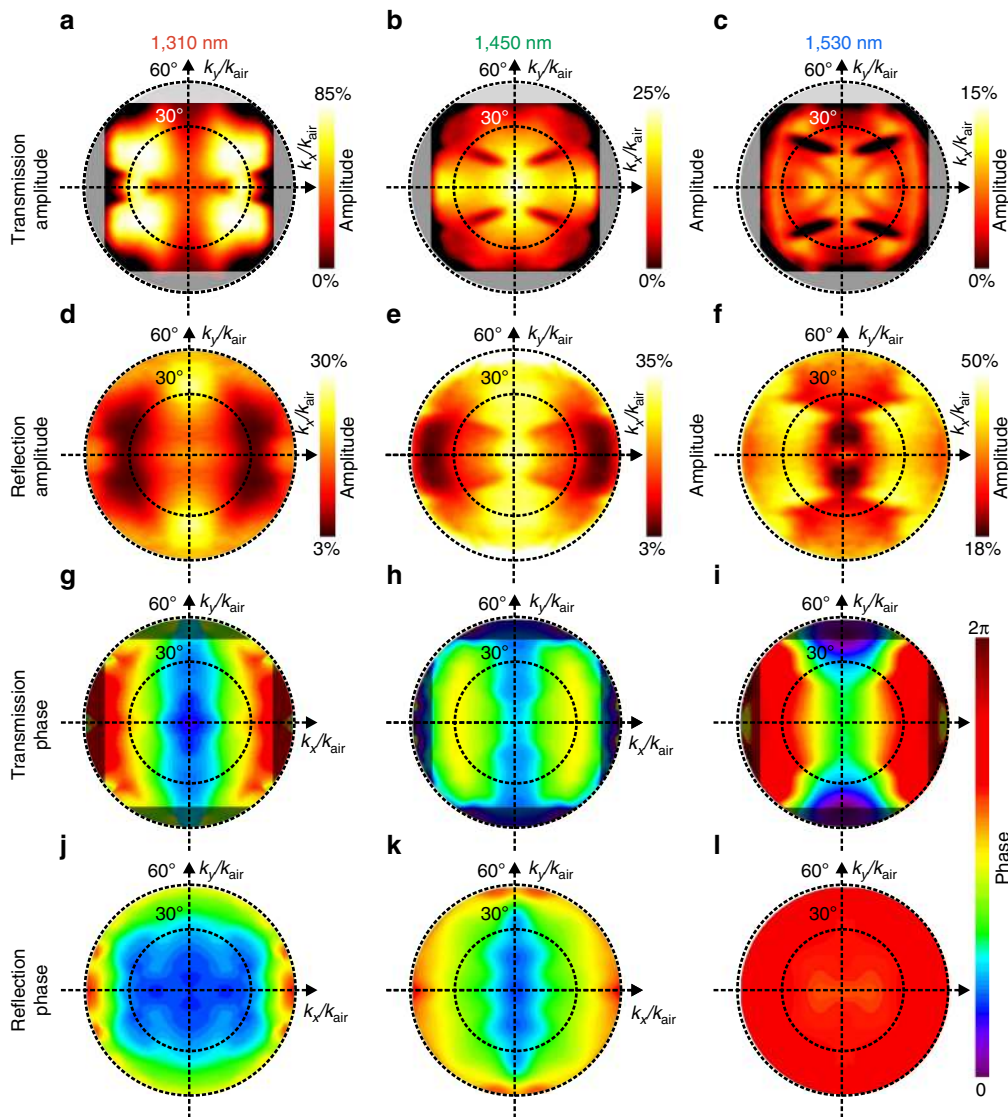


Figure 2 | Experimental results. Measured (a–c) transmission and (d–f) reflection amplitudes, (g–i) transmission and (j–l) reflection phase for three different wavelengths: (a,d,g,j) 1,310 nm, (b,e,h,k) 1,450 nm and (c,f,i,l) 1,530 nm. All the measurements are performed for the range of incident angles 0–60° and are plotted versus wave vector components k_x and k_y normalized by the length of the wave vector in air k_{air} . Horizontal axes correspond to TM-polarized illumination. Vertical axes correspond to TE illumination. Square apertures for the transmission amplitude and phase measurements show the numerical aperture limited by the size of the windows in the supporting silicon wafer.

we use a Mach–Zehnder-type interferometer²³, while for the measurements of a phase in reflection we employ a Michelson–Morley interferometer²³. To resolve transmission and reflection at different angles, we focus and collect the light using objective lens with high numerical aperture (Olympus LCPLN100XIR NA 0.85) and project the objective’s back-focal plane image onto an infrared camera (Xenics XS-1.7-320). The resulting image on the camera represents the \mathbf{k} -space spectrum of the fishnet metamaterial with the central point of the image corresponding to the \mathbf{k} -vectors normal to the fishnet’s surface. The edge of the image corresponds to \mathbf{k} -vectors oblique to the fishnet at an angle $\sim 58^\circ$, limited by the numerical aperture of the objective. We note that for transmission measurements the numerical aperture is limited to 0.7 by the finite size of the silicon nitride membrane window etched into the supporting silicon handle wafer. This restriction also assures insignificant non-paraxial effects due to the sharp focusing. To obtain the phase information, we interfere the back-focal plane image with a reference beam. To reconstruct the phase information from the

interference pattern, we employ off-axis digital holography technique²⁴ (see details in Supplementary Note 3).

We measure the complex transmission and reflection for the following three different wavelengths: 1,310, 1,450 and 1,530 nm, marked in Fig. 1b,c with red, green and blue, respectively. We notice that for the first wavelength, the metamaterial exhibits positive refractive index for normal incidence of light; for the second wavelength, the refractive index is close to zero and for the latter wavelength, the refractive index is negative (Fig. 1c). The results of our angular measurements are presented in Fig. 2. We use a linearly polarized light source with the electric field polarized in the x direction. After the objective lens, the focusing beam has TE polarization along the k_y axis and TM polarization along the k_x axis. As a result, the back-focal plane images (Fig. 2) contain information about the optical response of the sample with respect to both TE- and TM-polarized light along the k_y and k_x axes, respectively. We notice that the material’s magnetic dispersion is measured along the k_y axis, and the electric dispersion is measured along the k_x axis.

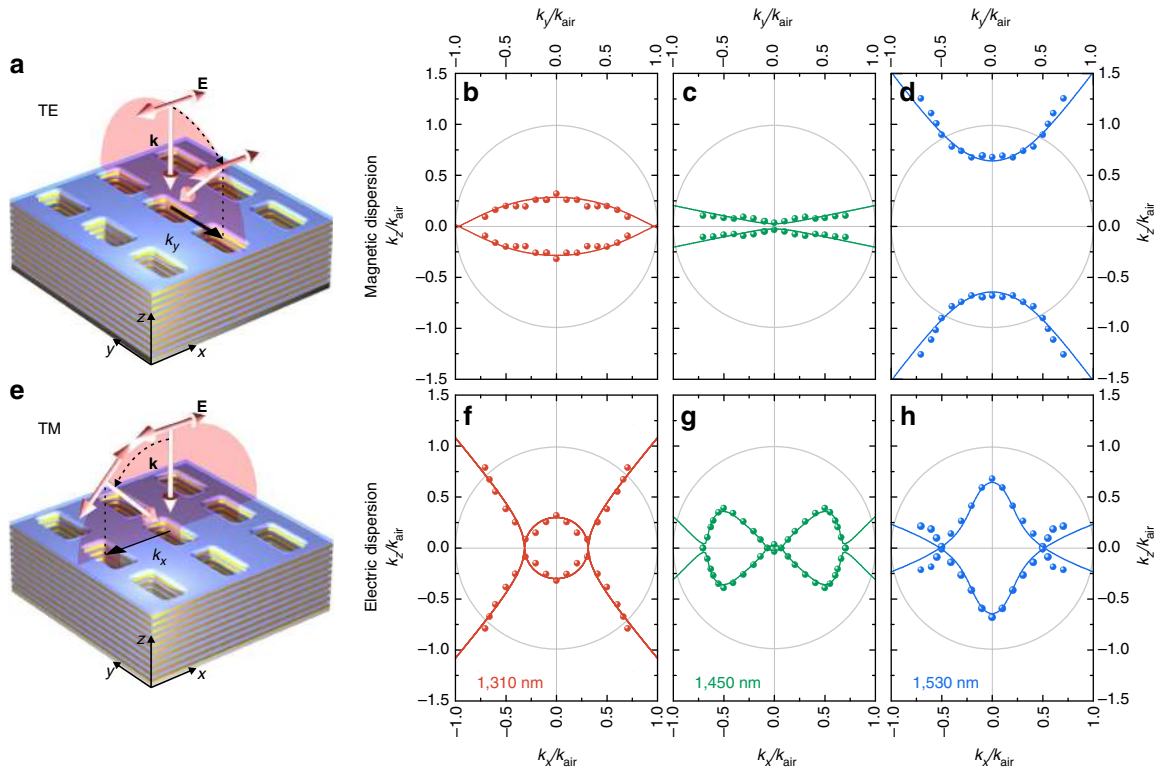


Figure 3 | Experimental observation of a transition from elliptic to hyperbolic dispersion. (a) Sketch of the TE illumination geometry showing relative orientations of the sample, wave vector \mathbf{k} and electric field \mathbf{E} . (b–d) Isofrequency dispersion contours for the TE polarization at wavelengths 1,310, 1,450 and 1,530 nm, respectively. Wave vector components k_y and k_z are normalized by the length of the wave vector in air k_{air} . (e) Sketch of the TM illumination geometry. (f–h) Isofrequency dispersion contours for the TM polarization at wavelengths 1,310, 1,450 and 1,530 nm, respectively. Dots mark experimental data, and lines correspond to analytical results. Grey circles correspond to the isofrequency contour of light in vacuum.

Table 1 | Effective parameters of the metamaterial dispersion.

Parameter	1,310 nm	1,450 nm*	1,530 nm
ϵ_x	$0.45 + i 0.8$	$-0.045 + i 0.03$	$-0.14 + i 0.25$
ϵ_z	$0.2 + i 0.01$	$0.08 + i 0.002$	$-0.02 + i 0.023$
μ_y	$0.18 + i 0.3$	$0.06 + i 0.13$	$-2 + i 0.1$
μ_z	1	1	1

*Nonlocal parameters at 1,450 nm wavelength $\partial^2 \epsilon_x / \partial k_x^2 = 7$, $\partial^2 \epsilon_z / \partial k_x^2 = 0.82$ and $\partial^2 \epsilon_z / \partial k_z^2 = 0$.

From our measurements, we can see that for a specific range of angles of incidence at 1,310 nm and 1,450 nm wavelengths, the reflection becomes $< 4\%$, which, for comparison, is lower than the reflection of glass. This is a direct consequence of the impedance matching of the metamaterial to air.

Next, we analyse the phase accumulation of light inside the metamaterial (Fig. 2g–i). At 1,310 nm wavelength (Fig. 2g), the phase accumulation increases from the centre (normal incidence) to the edges (60° oblique incidence). This is similar to the response of a usual dielectric, where the phase accumulation increases with a growth of an optical path inside the material. At 1,450 nm wavelength, the phase accumulation along the k_y axis remains nearly unchanged being close to zero for the entire range of incident angles. This corresponds to the case of ϵ -near-zero²⁵ and μ -near-zero²⁶ materials. Finally, at 1,530 nm wavelength, the phase accumulation is decreasing from the centre to the edges along the k_y axis, while it is increasing along the k_x axis.

Isofrequency analysis. Next, we reconstruct the isofrequency contours out of the measured transmission and reflection data

(see details in Supplementary Note 2). For the three wavelengths and two polarizations, these dispersion contours are shown in Fig. 3b–d,f–h.

We use an analytical approach to reveal the shapes of isofrequency surfaces obtained experimentally. We write explicitly a set of two equations for two principal linear polarizations: TE and TM. Without a lack of generality, we assume that for TE polarization the electric field component is pointing in the x direction, and for TM polarization the magnetic field component is pointing in the y direction. The resulting dispersion relations take the form:

$$\begin{aligned} \text{TE: } & \frac{k_y^2}{\epsilon_x \mu_z} + \frac{k_z^2}{\epsilon_x \mu_y} = \frac{\omega^2}{c^2}; \\ \text{TM: } & \frac{k_x^2}{\epsilon_z \mu_y} + \frac{k_z^2}{\epsilon_x \mu_y} = \frac{\omega^2}{c^2}. \end{aligned} \quad (1)$$

Thus, the material response is described by a set of parameters ϵ_x , ϵ_z , μ_y and μ_z . For the case of purely real values of parameters (for example, for materials with no loss or gain), the dispersion equations describe two types of isofrequency contours: either elliptic or hyperbolic depending on the relative signs of the parameters. In particular, opposite signs of the electric permittivity components ϵ_x and ϵ_z lead to hyperbolic isofrequency contours for TM polarization, while the opposite signs of the magnetic permeability components μ_y and μ_z lead to hyperbolic isofrequency contours for the TE polarization. Here we take into account the absorption of light in the metamaterial and consider the parameters ϵ_x , ϵ_z and μ_y as complex numbers with the imaginary parts representing losses. We assume $\mu_z = 1$ for all the cases, as we do not expect artificial magnetic response

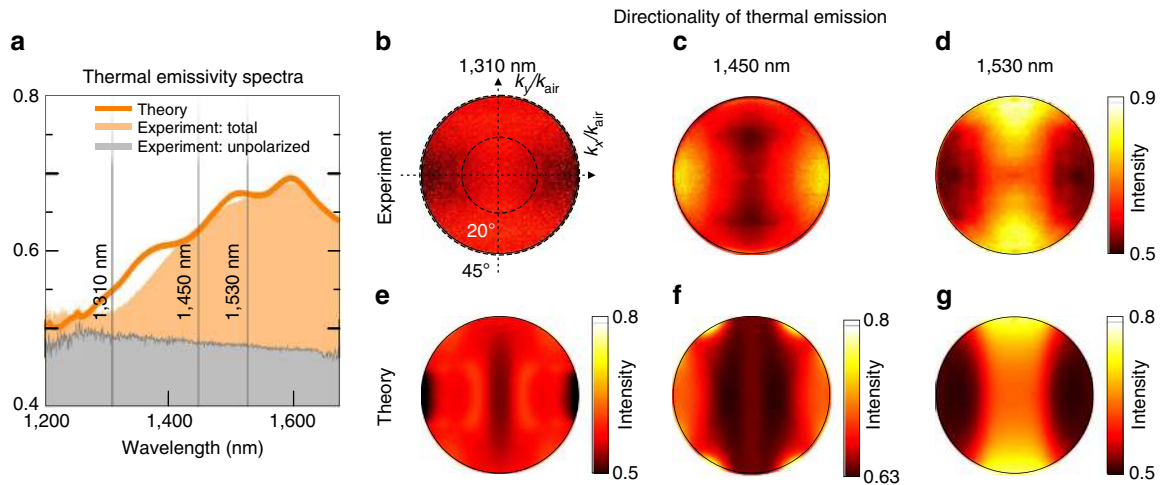


Figure 4 | Thermal emission from bulk magnetic hyperbolic metamaterials. (a) Spectrum of thermal emission normalized by the black body spectrum (emissivity). The unpolarized portion of emission is shown in grey, whereas the total emissivity is shown in orange above the unpolarized part. Line represents the corresponding theoretical calculation for the total emissivity. (b–d) Experimentally measured directionality of thermal emissivity at wavelengths 1,310, 1,450 and 1,530 nm, respectively, plotted versus wave vector components k_x and k_y normalized by the length of the wave vector in air k_{air} . (e–g) Theoretically calculated directionality for the same three wavelengths, respectively. Images (c–g) have the same coordinate system as b.

from the structure in the z direction. Table 1 summarizes the values of ϵ_x , ϵ_z and μ_y used in our analytical model to describe the experimental data.

As we observe, at 1,310 nm wavelength (Fig. 3b,f), all the material parameters have positive real parts, thus representing the cases of the elliptic dispersion. Interestingly, in both cases, the shapes of the isofrequency contours deviate from elliptical. This effect comes from the imaginary parts of ϵ_x , ϵ_z and μ_y . It is known that finite material losses lead to a hybridization of propagating and evanescent modes²⁷. Importantly, in our case for the TM polarization (see Fig. 3f), the hybridization leads to a new class of topology of isofrequency contours that is different from either elliptic or hyperbolic.

At 1,530 nm wavelength and TE polarization, the permeability coefficient μ_y has a negative real part, which is opposite to the sign of the permeability coefficient $\mu_z = 1$. Therefore, in this spectral region, the material dispersion becomes magnetic hyperbolic (see Fig. 3d). The branches of the hyperbola go beyond the isofrequency contour of light in air. We notice that the \mathbf{k} -vectors with tangential components larger than $|k_{\text{air}}|$ are not accessible experimentally when the metamaterial is illuminated from free space. However, an analytical extrapolation of the experimental curves supports the existence of propagating waves with large wave vectors. This is a key to achieve extraordinary optical properties of hyperbolic media, such as super-resolution imaging, nanoscale optical cavities and control over the density of photon states. For the other TM polarization, however, all three material parameters ϵ_x , ϵ_z and μ_y are simultaneously negative resulting in elliptic dispersion with a complex topology of isofrequency contours due to the presence of losses (see Fig. 3h).

At 1,450 nm wavelength, the parameters ϵ_x , ϵ_z and μ_y are vanishing simultaneously, representing the regime of optical topological transition². Around the topological transition, ϵ_x , ϵ_z and μ_y change their signs due to the resonant nature of the metamaterial's response. This results in an increase of the phase velocity of light towards infinity inside the structure. Importantly, at this wavelength, the structure supports propagating waves with \mathbf{k} -vectors substantially smaller than the \mathbf{k} -vectors in air, while all conventional optical materials support \mathbf{k} -vectors larger than those in air. As local material parameters become close to zero, we expect to see strong contributions from nonlocal response of the

metamaterials²⁸. This implies that the permittivity coefficients ϵ_x and ϵ_z become functions of the wave vector \mathbf{k} (see details in Supplementary Note 4). We find that for the magnetic (TE) dispersion of the fishnet metamaterials, both local and nonlocal models result in the same dispersion relation. Therefore, we consider the electric (TM) dispersion equation only, which in the nonlocal case takes the form:

$$\text{TM: } \frac{k_x^2}{\epsilon_z + \frac{\partial^2 \epsilon_z}{\partial k_x^2} k_x^2 + \frac{\partial^2 \epsilon_z}{\partial k_z^2} k_z^2} + \frac{k_z^2}{\epsilon_x + \frac{\partial^2 \epsilon_x}{\partial k_x^2} k_x^2 + \frac{\partial^2 \epsilon_x}{\partial k_z^2} k_z^2} = \frac{\omega^2}{c^2} \quad (2)$$

We notice that $\mu_y = (1 - \omega^2/c^2 \partial^2 \epsilon_x / \partial k_z^2)^{-1}$ (ref. 28). We further neglect the nonlocal parameter $\partial^2 \epsilon_z / \partial k_z^2$, as we find it to be of a minor importance²⁸. Thus, for the case of 1,450 nm wavelength, near the point of the optical topological transition of the metamaterial, we introduce two extra spatially dispersive terms $\partial^2 \epsilon_x / \partial k_x^2$ and $\partial^2 \epsilon_z / \partial k_x^2$ to describe the experimental dispersion. The values of the material parameters for the 1,450 nm wavelength are also given in Table 1. Our results suggest that a wide range of nontrivial isofrequency dispersion contours can be realized by an appropriate tuning of material's loss, gain and spatial dispersion. While all possible types of isofrequency contours for local media without loss/gain are limited to the second-order geometrical curves²⁹ (such as an ellipse or hyperbola), the presence of loss, gain and spatial dispersion extends the possible cases of isofrequency contours to the fourth-order curves. This leads to new topologies of the metamaterial dispersion.

In addition, we use full-wave numerical simulations to calculate material's isofrequency contours (see details in Supplementary Note 5 and Supplementary Fig. 1). We find that numerical results are in a good agreement with both experimental measurements and analytical calculations.

Manipulation of thermal emission from fishnet metamaterials.

Next, we study the effect of hyperbolic dispersion on far-field thermal emission. In our experiments, we heat the sample up to 400 °C with a ceramic heater. At this temperature, the metamaterial gives relatively bright thermal emission in the spectral region of interest, and it remains undamaged by heating. We collect the thermal emission of the fishnet metamaterial sample

by an objective lens with 10 mm working distance and 0.7 numerical aperture. In our experiments, we ensure that only thermal emission from the metamaterial sample is collected by the objective lens. We then direct it onto an infrared spectrometer and measure the thermal emission spectra. We take a reference measurement of the thermal emission from a silicon sample next to the fishnet metamaterial. The reference measurement allows us to find emissivity of fishnets (radiation of fishnets normalized by the black body radiation) using the known emissivity of silicon³⁰ and, in particular, characterize the degree of polarization of the emitted light (see details in Supplementary Note 6 and Supplementary Figs 2 and 3). We then measure the polarization states of the emissivity by employing Stokes vector formalism (see details in Supplementary Note 6 and Supplementary Figs 4 and 5). We find that in the spectral region with the magnetic elliptic dispersion, the thermal emission remains largely unpolarized. However, the degree of polarized light grows rapidly as we approach the point of the optical topological transition. In the spectral region of the magnetic hyperbolic dispersion, the thermal emission becomes partially linearly polarized. Figure 4a shows the emissivity spectrum of our sample. We notice that the unpolarized fraction of the emissivity remains almost unchanged over the measurement spectral range. The polarized part of the emission, however, increases at around the topological transition region and in the region with hyperbolic dispersion. These phenomena can be explained only by the enhanced density of photon states due to the magnetic hyperbolic dispersion. In addition, we argue that our far-field results suggest that the near-field thermal radiation can be characterized as super-Planckian, that is, exceeding the black body limit³¹.

Further, we study directionality of thermal emission at the three wavelengths of 1,310 nm, 1,450 and 1,530 nm. For this, we translate the back-focal plane image of the collecting objective onto the infrared camera through a corresponding band-pass filter. We again employ Stokes formalism to characterize the polarization states of directionality diagrams (details of the back-focal plane polarimetry method can be found in ref. 32). With this method, we retrieve the polarized portion of the thermal emission and plot its directionality diagrams for the three wavelengths in Fig. 4b–d. We notice that the directionality of emission at 1,310 nm (elliptic dispersion) is not pronounced, while the emission at 1,530 nm has a noticeable north–south directionality. Importantly, the directions of high thermal radiation correspond to the directions with large \mathbf{k} -vectors on the magnetic hyperbolic dispersion curve in Fig. 3d. Emission at the point of topological transition exhibits noticeable directionality as well; in particular, the emission in the direction normal to the sample is suppressed (the centre of the image in Fig. 4c). This corresponds to the region with near-zero \mathbf{k} -vectors. The fact that in the regime of the magnetic hyperbolic dispersion, the thermal emission is directional implies that it exhibits a high degree of spatial coherence.

We further calculate the spectra and directionalities of thermal emission theoretically (see details in Supplementary Note 7). The results of our calculations are shown in Fig. 4a with a line for the spectral density and Fig. 4e–g for the directionality. The calculated spectra and directionality diagrams show an excellent qualitative agreement with our experimental measurements.

In addition, we compare experimental thermal emission directionalities at 400 °C with experimentally measured absorption directionalities at room temperature (see details in Supplementary Note 6 and Supplementary Fig. 6). The directionalities look similar, while resembling some differences in details associated with the change of material properties with temperature.

Discussion

We have demonstrated experimentally optical magnetic hyperbolic metamaterial with the principal components of the magnetic permeability tensor having the opposite signs. We have developed an experimental method for direct measurements of isofrequency dispersion contours of three-dimensional metamaterials and directly observed a topological transition between the elliptic and hyperbolic dispersions in metamaterials. In the hyperbolic regime, the length of wave vectors inside the metamaterial is diverging towards infinity.

We have applied an analytical theory that takes into account losses and spatial dispersion to describe the measured isofrequency contours, and demonstrated the importance of nonlocal contributions³³ in the regime of optical topological transitions, associated with vanishing local parameters. A control of loss, gain and spatial nonlocalities in metamaterials opens up new opportunities for engineering isofrequency dispersion contours beyond elliptic or hyperbolic, with nontrivial geometry and topology. The magnetic hyperbolic dispersion of metamaterials together with their electric response enables impedance matching between hyperbolic media and air, resulting in an efficient light transfer through interfaces. Our results suggest that other three-dimensional metamaterials assembled from magnetically polarizable or chiral elements^{34–36} may possess magnetic hyperbolic dispersion as well.

In addition, we have studied the effect of the hyperbolic dispersion on thermal emission of metamaterials, and revealed that the magnetic hyperbolic metamaterial demonstrates enhanced, directional, coherent and polarized thermal emission. These results suggest an advanced thermal management that can find applications in thermophotovoltaics³⁷, scanning thermal microscopy³⁸, coherent thermal sources³⁹ and other thermal devices.

Methods

Nanofabrication. The bulk fishnet metamaterial is fabricated on a suspended 50-nm low-stress silicon nitride (Si_3N_4) membrane made from standard microelectromechanical systems fabrication technologies. The metal–dielectric stack is then deposited onto the Si_3N_4 membrane using layer-by-layer electron beam evaporation technique at pressure $\sim 1 \times 10^{-6}$ Torr without vacuum break. The chamber temperature is cooled down on each layer of evaporation to avoid buildup of excessive heating and stress. Essentially 10 repeating layers of gold (Au, 30 nm) and magnesium fluoride (MgF_2 , 45 nm) are deposited. Next, the sample is turned upside down and mounted on a special stage holder, which has a matching trench that prevents any mechanical contact with the fragile multilayer structure sitting on the membrane. The nanostructures are milled by gallium (Ga) focused ion beam from the membrane side. Milling from the membrane side prevents the implantation of Ga ions into the metal layers at the unpatterned areas that reduces optical losses and improves the overall quality. This is essential to mask the implantation of Ga ions into the metal layers at the unpatterned areas. The final structure has a slight sidewall angle along the thickness direction, but is found to have minor influence on the optical properties. Another important advantage of focused ion beam fabrication of the structure on a thin membrane compared with conventional bulk substrates is the ability for Ga ions to enter the free space (that is, no substrate for Ga ions to accumulate and cause undesired contamination and absorption).

References

1. Smith, D. & Schurig, D. Electromagnetic wave propagation in media with indefinite permittivity and permeability tensors. *Phys. Rev. Lett.* **90**, 077405 (2003).
2. Krishnamoorthy, H. N., Jacob, Z., Narimanov, E., Kretzschmar, I. & Menon, V. M. Topological transitions in metamaterials. *Science* **336**, 205–209 (2012).
3. Poddubny, A., Iorsh, I., Belov, P. & Kivshar, Y. Hyperbolic metamaterials. *Nat. Photon.* **7**, 948–957 (2013).
4. Yao, J. *et al.* Optical negative refraction in bulk metamaterials of nanowires. *Science* **321**, 930–930 (2008).
5. Noginov, M. *et al.* Bulk photonic metamaterial with hyperbolic dispersion. *Appl. Phys. Lett.* **94**, 151105 (2009).
6. Kabashin, A. *et al.* Plasmonic nanorod metamaterials for biosensing. *Nat. Mater.* **8**, 867–871 (2009).

7. Kanungo, J. & Schilling, J. Experimental determination of the principal dielectric functions in silver nanowire metamaterials. *Appl. Phys. Lett.* **97**, 021903 (2010).
8. Noginov, M. *et al.* Controlling spontaneous emission with metamaterials. *Opt. Lett.* **35**, 1863–1865 (2010).
9. Wurtz, G. A. *et al.* Designed ultrafast optical nonlinearity in a plasmonic nanorod metamaterial enhanced by nonlocality. *Nat. Nanotechnol.* **6**, 107–111 (2011).
10. Sun, J., Litchinitser, N. M. & Zhou, J. Indefinite by nature: from ultraviolet to terahertz. *ACS Photon.* **1**, 293–303 (2014).
11. Dai, S. *et al.* Tunable phonon polaritons in atomically thin van der waals crystals of boron nitride. *Science* **343**, 1125–1129 (2014).
12. Smith, D. R., Kolinko, P. & Schurig, D. Negative refraction in indefinite media. *J. Opt. Soc. Am. B* **21**, 1032–1043 (2004).
13. Hussain, R. *et al.* Enhancing $eu_3 +$ magnetic dipole emission by resonant plasmonic nanostructures. *Opt. Lett.* **40**, 1659–1662 (2015).
14. Kasperczyk, M., Person, S., Ananias, D., Carlos, L. D. & Novotny, L. Excitation of magnetic dipole transitions at optical frequencies. *Phys. Rev. Lett.* **114**, 163903 (2015).
15. Jacob, Z., Alekseyev, L. V. & Narimanov, E. Optical hyperlens: far-field imaging beyond the diffraction limit. *Opt. Express* **14**, 8247–8256 (2006).
16. Liu, Z., Lee, H., Xiong, Y., Sun, C. & Zhang, X. Far-field optical hyperlens magnifying sub-diffraction-limited objects. *Science* **315**, 1686–1686 (2007).
17. Soukoulis, C. M. & Wegener, M. Past achievements and future challenges in the development of three-dimensional photonic metamaterials. *Nat. Photon.* **5**, 523–530 (2011).
18. Sun, J. *et al.* Low loss negative refraction metamaterial using a close arrangement of split-ring resonator arrays. *New J. Phys.* **12**, 083020 (2010).
19. Shchelokova, A. V., Filonov, D. S., Kapitanova, P. V. & Belov, P. A. Magnetic topological transition in transmission line metamaterials. *Phys. Rev. B* **90**, 115155 (2014).
20. Valentine, J. *et al.* Three-dimensional optical metamaterial with a negative refractive index. *Nature* **455**, 376–379 (2008).
21. Kruk, S. S., Powell, D. A., Minovich, A., Neshev, D. N. & Kivshar, Y. S. Spatial dispersion of multilayer fishnet metamaterials. *Opt. Express* **20**, 15100–15105 (2012).
22. O'Brien, K. *et al.* Reflective interferometry for optical metamaterial phase measurements. *Opt. Lett.* **37**, 4089–4091 (2012).
23. Saleh, B. & Teich, M. *Wiley Series in Pure and Applied Optics* (Wiley, 2007).
24. Cuche, E., Marquet, P. & Depeursinge, C. Simultaneous amplitude-contrast and quantitative phase-contrast microscopy by numerical reconstruction of fresnel off-axis holograms. *Appl. Opt.* **38**, 6994–7001 (1999).
25. Alù, A., Silveirinha, M. G., Salandrino, A. & Engheta, N. Epsilon-near-zero metamaterials and electromagnetic sources: Tailoring the radiation phase pattern. *Phys. Rev. B* **75**, 155410 (2007).
26. Engheta, N. & Ziolkowski, R. *Metamaterials: Physics and Engineering Explorations* (Wiley, 2006).
27. Davoyan, A. R. *et al.* Mode transformation in waveguiding plasmonic structures. *Photon. Nanostruct. Fundam. Appl.* **9**, 207–212 (2011).
28. Gorlach, M. A. & Belov, P. A. Nonlocality in uniaxially polarizable media. *Phys. Rev. B* **92**, 085107 (2015).
29. Berger, M., Cole, M. & Levy, S. *Geometry II. Universitext* (Springer, 2009).
30. Ravindra, N. *et al.* Emissivity measurements and modeling of silicon-related materials: an overview. *Int. J. Thermophys.* **22**, 1593–1611 (2001).
31. Guo, Y., Cortes, C. L., Molesky, S. & Jacob, Z. Broadband super-planckian thermal emission from hyperbolic metamaterials. *Appl. Phys. Lett.* **101**, 131106 (2012).
32. Kruk, S. S. *et al.* Spin-polarized photon emission by resonant multipolar nanoantennas. *ACS Photon.* **1**, 1218–1223 (2014).
33. Orlov, A. A., Voroshilov, P. M., Belov, P. A. & Kivshar, Y. S. Engineered optical nonlocality in nanostructured metamaterials. *Phys. Rev. B* **84**, 045424 (2011).
34. Liu, N. *et al.* Three-dimensional photonic metamaterials at optical frequencies. *Nat. Mater.* **7**, 31–37 (2008).
35. Pendry, J. A chiral route to negative refraction. *Science* **306**, 1353–1355 (2004).
36. Gansel, J. K. *et al.* Gold helix photonic metamaterial as broadband circular polarizer. *Science* **325**, 1513–1515 (2009).
37. Lenert, A. *et al.* A nanophotonic solar thermophotovoltaic device. *Nat. Nanotechnol.* **9**, 126–130 (2014).
38. De Wilde, Y. *et al.* Thermal radiation scanning tunnelling microscopy. *Nature* **444**, 740–743 (2006).
39. Greffet, J.-J. *et al.* Coherent emission of light by thermal sources. *Nature* **416**, 61–64 (2002).

Acknowledgements

We thank D. Smith and D. Basov for discussions and also acknowledge useful suggestions from S. Fan and C. Simovski. The work was partially supported by the Australian Research Council. Z.J.W., K.O. and X.Z. were funded by the Director, Office of Science, Office of Basic Energy Sciences, Materials Sciences and Engineering Division, of the U.S. Department of Energy under Contract No. DE-AC02-05-CH11231.

Author contributions

S.S.K., D.N.N. and Y.S.K. conceived the idea. S.S.K. conducted the experiments. E.P.-S. assisted with the spatially resolved interferometric measurements. Z.J.W., K.O.B. and X.Z. designed the samples. Z.J.W. fabricated the samples. Z.J.W. and K.O.B. conducted sample quality control. S.S.K. performed the analytical modelling and numerical simulations. S.S.K. and Y.S.K. wrote the manuscript. S.S.K., Z.J.W., K.O.B., D.N.N., Y.S.K. and X.Z. analysed the experimental and theoretical results. All authors contributed to discussions and edited the manuscript.

Additional information

Supplementary Information accompanies this paper at <http://www.nature.com/naturecommunications>

Competing financial interests: The authors declare no competing financial interests.

Reprints and permission information is available online at <http://npg.nature.com/reprintsandpermissions/>

How to cite this article: Kruk, S. S. *et al.* Magnetic hyperbolic optical metamaterials. *Nat. Commun.* **7**:11329 doi: 10.1038/ncomms11329 (2016).



This work is licensed under a Creative Commons Attribution 4.0 International License. The images or other third party material in this article are included in the article's Creative Commons license, unless indicated otherwise in the credit line; if the material is not included under the Creative Commons license, users will need to obtain permission from the license holder to reproduce the material. To view a copy of this license, visit <http://creativecommons.org/licenses/by/4.0/>